


Ultracoherent Nanomechanical Resonators Based on Density Phononic Crystal Engineering

Dennis Høj[✉],* Ulrich Busk Hoff[✉], and Ulrik Lund Andersen[†]

Center for Macroscopic Quantum States (bigQ), Department of Physics, Technical University of Denmark, Fysikvej, 2800 Kongens Lyngby, Denmark

 (Received 9 January 2023; revised 9 December 2023; accepted 22 December 2023; published 6 March 2024)

Micromechanical and nanomechanical systems with exceptionally low dissipation rates are enabling the next-generation technologies of ultrasensitive detectors and quantum information systems. New techniques and methods for lowering the dissipation rate have in recent years been discovered and allowed for the engineering of mechanical oscillators with phononic modes that are extremely well isolated from the environment and thus possess quality factors close to and beyond 1×10^9 . A powerful strategy for isolating and controlling a single phononic mode is based on phononic crystal engineering. Here we propose a new method for phononic crystal engineering of nanomechanical oscillators that is based on a periodic variation of the material density. To circumvent the introduction of additional bending losses resulting from the variation of material density, the added mass constitutes an array of nanopillars in which the losses will be diluted. Using this novel technique for phononic crystal engineering, we design and fabricate corrugated mechanical oscillators with quality factors approaching 1×10^9 in a room temperature environment. The flexibility space of these new phononic crystals is large and further advancement can be attained through optimized phononic crystal patterning and strain engineering via topology optimization. This will allow for the engineering of mechanical membranes with quality factors beyond 1×10^9 at room temperature. Such extremely low mechanical dissipation rates will enable the development of radically new technologies such as quantum-limited atomic force microscopy at room temperature, ultrasensitive detectors of dark matter, spontaneous waveform collapses, gravity, and high-efficiency quantum information transducers.

DOI: [10.1103/PhysRevX.14.011039](https://doi.org/10.1103/PhysRevX.14.011039)

Subject Areas: Condensed Matter Physics,
Mechanics, Nanophysics

I. INTRODUCTION

Micro- and nanomechanical systems exhibiting remarkably low dissipation rates have emerged as pivotal enablers for cutting-edge technologies, particularly in the realms of ultrasensitive detectors and quantum information systems [1]. This unprecedentedly low mechanical dissipation holds the promise of revolutionizing various technological frontiers, including the realization of quantum-limited atomic force microscopy at room temperature, ultrasensitive detectors for dark matter investigations [2], studies of spontaneous waveform collapses [3], investigations into gravity [4], and the development of high-efficiency quantum information transducers [5].

Over the past decade, significant strides have been made in the field, particularly through the utilization of

stoichiometric silicon nitride. This material, owing to its inherent extremely high tensile stress, has paved the way for the construction of mechanical resonators in diverse forms such as strings, membranes, and trampolines, all demonstrating ultralow dissipation [6–17]. Recent breakthroughs in dissipation rate reduction techniques and methodologies have facilitated the engineering of mechanical oscillators with phononic modes that exhibit exceptional isolation from their environment, resulting in quality factors approaching and surpassing 1 billion. A particularly potent strategy for isolating and controlling a single phononic mode involves the emerging field of phononic crystal engineering [18–23].

Phononic crystal engineering is an extremely powerful method for controlling the phononic properties of material systems in much the same way as photonic crystals are able to control light [24,25]. The method is being used to engineer material systems for controlling heat and sound at both the macroscale and the microscale, for example, with applications in the design of loudspeakers and microphones to control the direction of sound [26], in buildings and vehicles to isolate sound, and in communication technologies to enable signal processing at 5 G frequencies. In particular, in recent years, phononic crystals have been used

*denho@fysik.dtu.dk

†ulrik.andersen@fysik.dtu.dk

Published by the American Physical Society under the terms of the Creative Commons Attribution 4.0 International license. Further distribution of this work must maintain attribution to the author(s) and the published article's title, journal citation, and DOI.

to control and isolate specific phononic modes of nano-mechanical and micromechanical resonators, protecting them from the surrounding thermal heat bath [18,19]. This has given rise to a completely new generation of ultracoherent mechanical oscillators with quality factors reaching 1×10^9 at room temperature.

The effect of enhancing the quality factor of mechanical resonators using phononic crystals is twofold. First, as a result of the periodic phononic structure, an acoustic band gap is formed in which phononic modes are trapped and thus unable to radiate into the surrounding environment that otherwise would cause dissipation [20,21,27]. Second, the phononic crystal structure can also be engineered to reduce the phononic mode curvature of the resonator at the clamping points to the substrate [7,10], which will lead to a decrease in the intrinsic dissipation rate for highly stressed systems—a technique that is known as soft clamping [18,19]. Phononic crystal membranes and strings exploiting these effects in harmony have been fabricated, and the membranes have been used in a series of optomechanical experiments [28–30].

A phononic crystal in a mechanical membrane is traditionally engineered by mapping a periodic pattern of holes into a prestressed silicon membrane. This produces a periodic variation in the stress of the material across the membrane, which in turn creates a phononic band gap with isolated modes that are associated with the vibrations at a central “defect” of the pattern. As mentioned above, this leads to acoustic isolation as well as soft clamping of a particular mode, and thus very large quality factors. However, the stress of the material at the location of the high-quality mode is low, which means that the quality-enhancing effect of dissipation dilution [6,31,32] is not

optimally used, and therefore eventually bounds the quality factor of the system. The technique of strain engineering can in some geometries be applied to colocate a high-stress region with the mechanical motion [19], but in this particular phononic membrane, it seems not possible.

In this paper, we propose a new type of phononic crystal engineering of a nanomechanical and micromechanical resonator that offers a larger flexibility in the design of periodic patterns and in which the stress can be engineered. Our strategy for phononic crystal nanoengineering is based on the creation of a periodic variation in the mass density across the membrane. More specifically, we propose and demonstrate the mapping of a periodic hexagonal pattern with a central defect onto a membrane that consists of an array of nanopillars, resulting in a membrane with periodic pattern of cell domains each containing an array of nanopillars, as illustrated in Figs. 1(a)–1(c) (note that the central defect is not shown in the figure). Such a density phononic membrane enables the formation of a frequency band gap with modes that are highly shielded from the substrate (acoustic filtering) and it reduces the curvature of the mode amplitude toward the clamping points, thereby lowering the intrinsic dissipation losses (soft clamping). Moreover, the use of a fine mesh of nanopillars for controlling the mass density ensures low intrinsic bending dissipation at the pillars. We therefore expect the density phononic membranes to exhibit ultralow dissipation rates.

Intuitively, the simplest strategy for phononic crystal engineering via material density variation is to periodically add mass by depositing large pillars representing the cells of the phononic crystal pattern. Such a structure will in principle create a band gap (similar to a holey structure), but the structure will be too stiff and it will be strongly

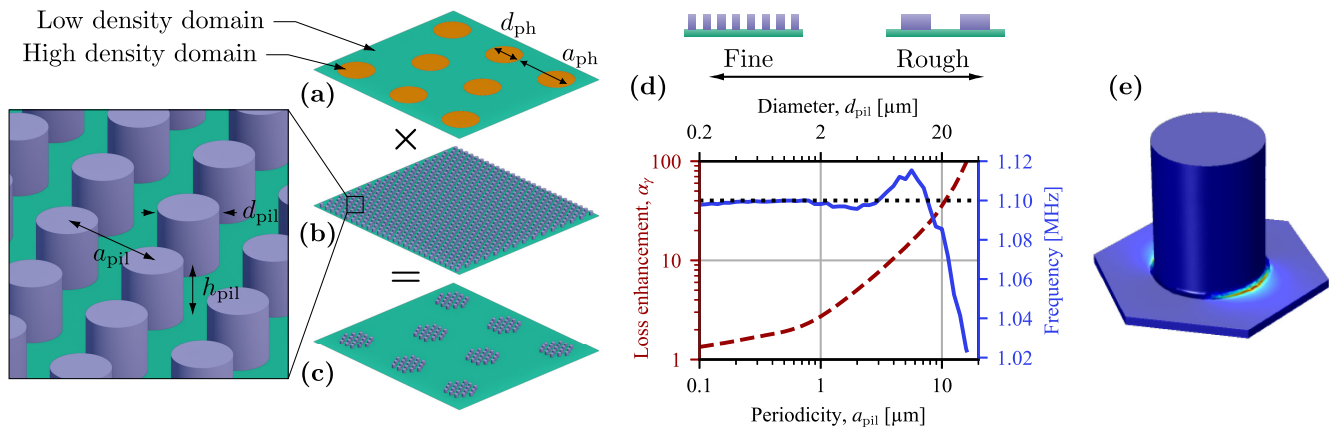


FIG. 1. Concept illustration. (a) The desired phononic crystal pattern of high and low material density regions. To approximate this behavior the distribution is used as a mask on top an even distribution of nanopillars shown in (b). The end result is an engineered distribution of nanopillars based on any desired material distribution as illustrated in (c). The enlarged inset of (b) highlights the relevant pillar parameters. (d) The increased losses relative to a hypothetical membrane (without pillars) of increased material density while keeping the total mass constant. It assumes a 20-nm-thick stoichiometric silicon nitride membrane vibrating at 1.1 MHz. The results are practically identical to the other studied frequencies. (e) Illustration of evanescent bending losses at the pillar base, estimated using 3D simulations.

affected by boundary bending losses at each of the domain walls. However, this stiffness and dissipation effect can be largely reduced by patterning a fine mesh of nanopillars within each of the cells. With such a strategy, the density contrast required for phononic engineering is kept while the bending loss is significantly reduced. This reduction is caused by the dilution of the loss into many nanopillars, each of which produces almost negligible loss due to their small diameter in comparison to the wavelength of the phononic mode. We simulate the potential loss enhancement (see Sec. II) by considering a hexagonal pattern of pillars on a membrane with the effective density,

$$\rho_{\text{eff}} = \rho \left(1 + \frac{\pi\sqrt{3}h_{\text{pil}}d_{\text{pil}}^2}{6ta_{\text{pil}}^2} \right), \quad (1)$$

where ρ is the density of the material (assuming the same material for membrane and pillars), while a_{pil} and h_{pil} are the diameter and height of the pillars, d_{pil} is the distance between them [see Fig. 1(b)], and t is the thickness of the membrane. The results of the simulations are presented in Fig. 1(d) where we plot the loss enhancement α_γ of a membrane patterned with a hexagonal array of pillars against the periodicity a_{pil} or pillar size d_{pil} (assuming $a_{\text{pil}} = 2d_{\text{pil}}$). It is clear that the intrinsic loss of the membrane is dramatically reduced by the introduction of

a nanopillar array, and for very small pillars, the loss contribution is effectively negligible.

Since the phononic crystal pattern is created by material density variation, there exists a large flexibility in defining its form and shape. Two examples are a binary and a sinelike pattern where the material density is changed either abruptly or smoothly across the membrane following a certain periodicity. Analytical expressions for these two patterns can be found in Appendix A. Furthermore, the flexibility of this design approach also allows the creation of nonuniform phononic crystals to further enhance the quality factor as well as mode confinement. See Appendixes B and C for a deeper analytical study of all designs. In the following, we interrogate the binary pattern. We assume the cell periodicity to be given by a_{ph} , the diameter of each cell to be d_{ph} , and the ratio $\alpha_w = d_{\text{ph}}/a_{\text{ph}}$. Furthermore we define the density contrast parameter, $g = \rho_{\text{eff}}/\rho$.

The optimization of the density phononic crystal is a trade-off between the size of the band gap, which should be as large as possible to encapsulate the mode of interest, and the dissipation of an isolated mode, which should be as low as possible. In Figs. 2(a) and 2(b) we present the results of simulating the relative band gap width and the quality factor of the isolated mode assuming that intrinsic losses are dominating. It is clear that the band gap becomes wider as the density contrast g increases as expected, and that an optimum is obtained for a specific relative distribution width α_w of around 0.4 (corresponding to $a_{\text{ph}} = 2.5d_{\text{ph}}$).

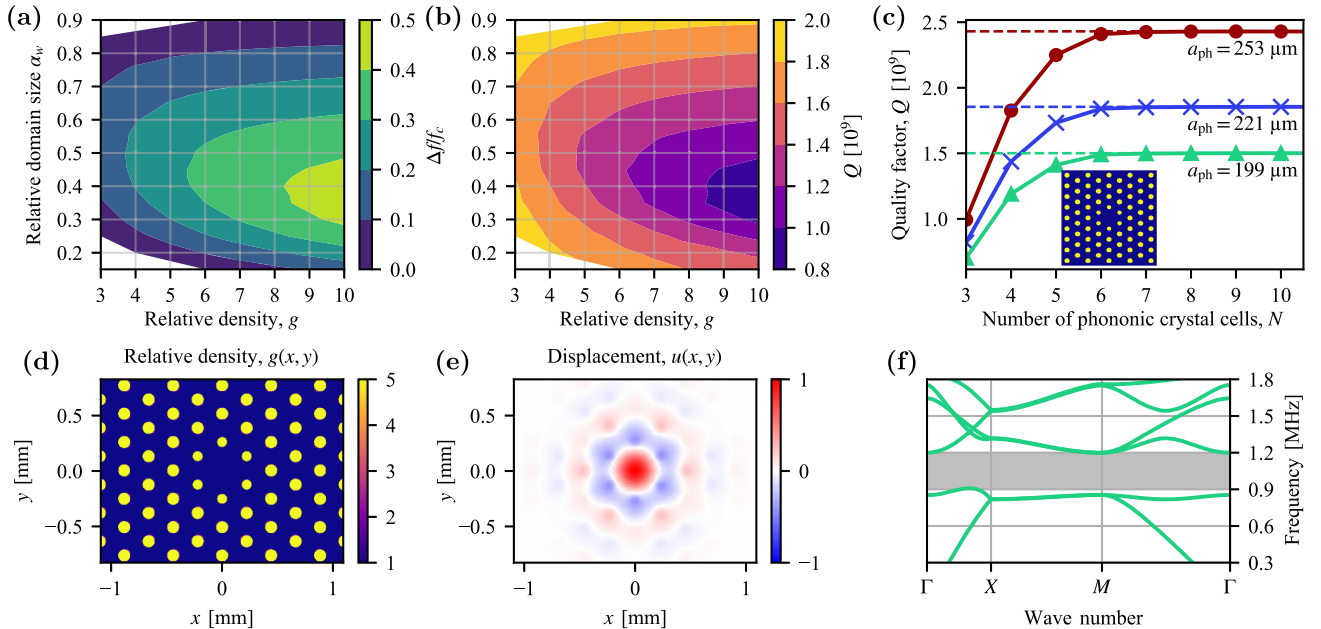


FIG. 2. Phononic analysis. Panels (a) and (b) show the relative band gap $\Delta f/f_c$ and quality factor Q , respectively, versus the phononic crystal contrast g and the relative domain size α_w (fixing the periodicity to $a_{\text{ph}} = 253 \mu\text{m}$ membrane). (c) Predicted quality factors versus number of isolating phononic crystal cell layers. The inset illustrates a membrane with $N = 4$. In panels (b) and (c), the Q factor was numerically estimated without accounting for the additional pillar loss (assuming very small pillars) and without accounting for acoustic radiation loss. Panels (d) and (e) illustrate the density distribution and the mode shape of the phononic membrane, respectively. (f) The band structure of the phononic crystal, where the shaded area highlights the band gap.

However, contrarily, the quality factor for the isolated mode is decreasing as the density contrast is increased. This is caused by the fact that a larger material density will lead to a smaller phase velocity and therefore a shorter wavelength of the propagating phononic mode. A shorter wavelength relative to the fixed size of the nanopillars will naturally lead to larger bending losses at the nanopillars, and thus a reduced quality factor. In the following, we choose a contrast of $g = 5$ which is a good compromise between having band gap of reasonable size and a large quality factor. In addition, based on these simulations, in the following we choose $\alpha_w = 0.4$.

To trap an isolated mode in the membrane, a defect is introduced simply by removing one of the cell domains. Such a disturbance in the phononic crystal allows some modes to occur in the band gap which will be spatially well confined at the defect. However, the resonance frequency of the high-quality mode is not centered in the band gap but at the lower end of it, which might lead to some mode leakage. To avoid this effect, we increase the frequency of the mode by lowering the material density of the phononic cells located just next to the defect. By choosing the contrast of these inner cells to $g = 3.9$ or the relative size to $\alpha_w = 0.32$, the frequency will be centered in the band gap. In Fig. 2, we show the contour of the density contrast [Fig. 2(d)], the displacement amplitude of the high-quality mode [Fig. 2(e)], and the dispersion relation that clearly exhibits the band gap [Fig. 2(f)]. Interestingly, we note that it generates a full band gap in contrast to stress-induced phononic membranes which produces a pseudo-band gap with in-plane modes [18]. Finally, in Fig. 2(c), we present the results of the simulated quality factor (based on intrinsic losses) for different number of layers of the phononic crystal cells as well as three different values for the periodicity of the

phononic pattern ($a_{\text{ph}} = 199, 221, 253 \mu\text{m}$). In these simulations we assume no added losses from the pillars ($\alpha_\gamma = 1$). The effect of soft clamping is clear. As more layers are added, the mode field curvature at the boundary is gradually reduced, which in turn leads to lower intrinsic dissipation rates, thereby increasing the quality factor. We see that at least 7 layers of phononic cells are required for saturating the quality factor to a value above 10^9 .

Our next step is to experimentally validate the expected quality of our proposed density phononic crystal. Toward this end, we fabricate membrane structures for different pillar periodicity and for different numbers of phononic cell layers. We fabricate the membranes from two thin layers of high-stress (about 1 GPa) silicon nitride films grown on a silicon wafer using low-pressure chemical vapor deposition (CVD) and plasma-enhanced CVD, respectively. Using UV lithography and reactive ion etching, the nanopillar pattern was transferred to the front side while a window for releasing the resonator was transferred to the back side. More details on the fabrication process can be found in Sec II.

We characterize the fabricated membranes by determining their frequency power spectrum as well as their quality factors using an interferometric ringdown measurement setup operating in ultrahigh vacuum to avoid air damping (see Sec. II). For the ringdown measurements, we excite the membrane by the exertion of radiation pressure force from a light beam modulated at the frequency of the mode under investigation, turn off the modulation, and subsequently record the decay of the membrane's motion using the same laser mode. An example of the measured power spectrum is illustrated in Fig. 3(c) and shows the clear existence of a band gap around the confined mode at 1.4 MHz. The result of the ringdown measurement of this particular mode is presented in Fig. 3(d) and yields a quality factor of 5.65×10^8 .

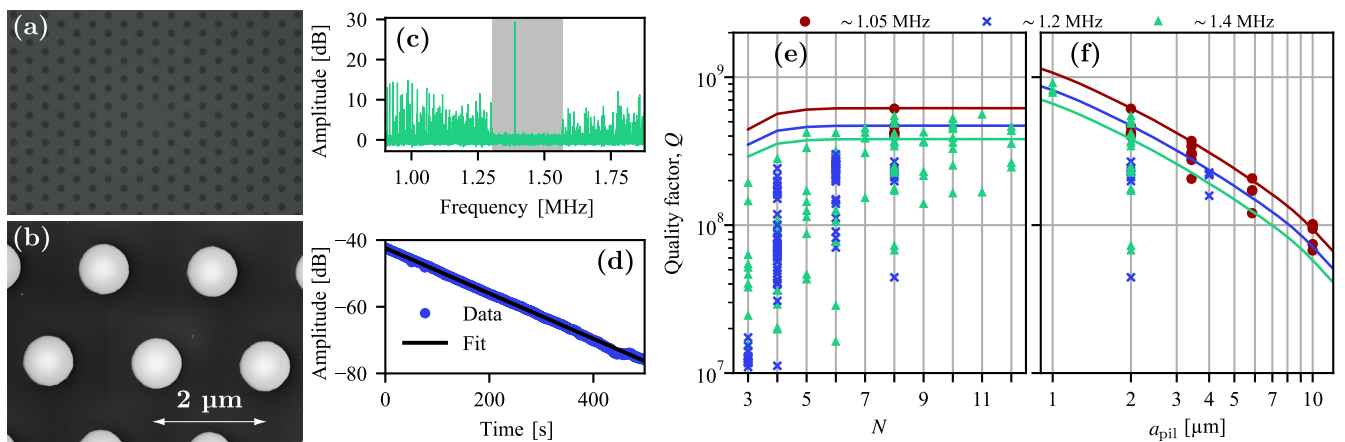


FIG. 3. Experimental results. (a) Microscope image of the fabricated density phononic membrane. (b) SEM image of the nanopillars of a specific membrane. (c) Spectrum of a density phononic membrane where the band gap region is highlighted by shaded gray. (d) An example of a ringdown measurement of a specific membrane exhibiting a Q factor of 5.65×10^8 . (e) Measured quality factors versus number of phononic cells N for $a_{\text{pil}} = 2 \mu\text{m}$. (f) Measured quality factor versus pillar periodicity a_{pil} for $N = 8$. The solid lines correspond to fitted simulation results based on the best samples.

In Fig. 3(e), we present the results for the measured quality factors of the band gap mode with different number of layers of phononic cells. As the number of cell layers increases, the quality factor improves since the increasing number of layers will gradually strengthen the effects of soft clamping and acoustic shielding against acoustic radiation losses. When the acoustic shielding is weak (that is, when only a few cell layers are present), the coupling to the surrounding substrate mode becomes stochastic, resulting in a large spread of the quality factors. For a large number of cell layers ($N_{\text{ph}} \geq 9$), the acoustic shielding effect becomes more effective and the spread is low. In Fig. 3(e), we compare the measured data with theory that accounts for intrinsic losses but neglecting acoustic radiation losses, and we clearly observe reasonable agreements to the best measured values.

Results for the quality factor of the band gap mode for different nanopillar periodicity a_{pil} are presented in Fig. 3(f). As we keep the phononic crystal pattern constant, a change in the periodicity effectively leads to a change in the nanopillar diameter ($d_{\text{pil}} = a_{\text{pil}}/2$) and density. As expected, the quality factor increases as we lower the periodicity (and thus the size of the nanopillars), as this will dilute the effect of bending losses at the pillars. We expect the quality factors to be limited by the intrinsic bending losses since we have chosen a large number of cell layers, $N_{\text{ph}} = 8$, diminishing the acoustic radiation losses. Indeed, by using a model that accounts only for intrinsic losses we obtain good agreement with the measured data, as shown in Fig. 3(f).

The smallest pillars that we were able to fabricate with the present fabrication method was around $1 \mu\text{m}$, which yields the maximum quality factor of 9.1×10^8 , and a Qf product of 1.3×10^{15} (corresponding to about 216 quantum coherent oscillations), which we believe is the largest reported Qf product at room temperature for membranes and similar to the best measured perimeter mode of a polygon-shaped resonator [17]. Moreover, according to our model, the quality factor will increase to beyond 1×10^9 by further decreasing the periodicity. Furthermore, due to the structural functionality of our system, it is possible to enhance the strain of the membrane and thereby further decrease the intrinsic losses through dissipation dilution. One particular strategy for increasing the stress is to use the design depicted in Fig. 4, where the stress of the central pad (on which the density phononic crystal could be located) is reaching approximately 2.1 GPa, thereby predicting a quality factor of 3.5×10^9 at 2 MHz (Qf product of 7×10^{15} Hz). In addition to improving the quality factor further by strain engineering, it is also possible to improve it by choosing optimized variations of the material density. For example, in the Supplemental Material we have considered a sinelike variation of the material density by which the quality factor is slightly improved. We have also investigated the possibility of varying the size and density of each phononic crystal cell, thereby creating a

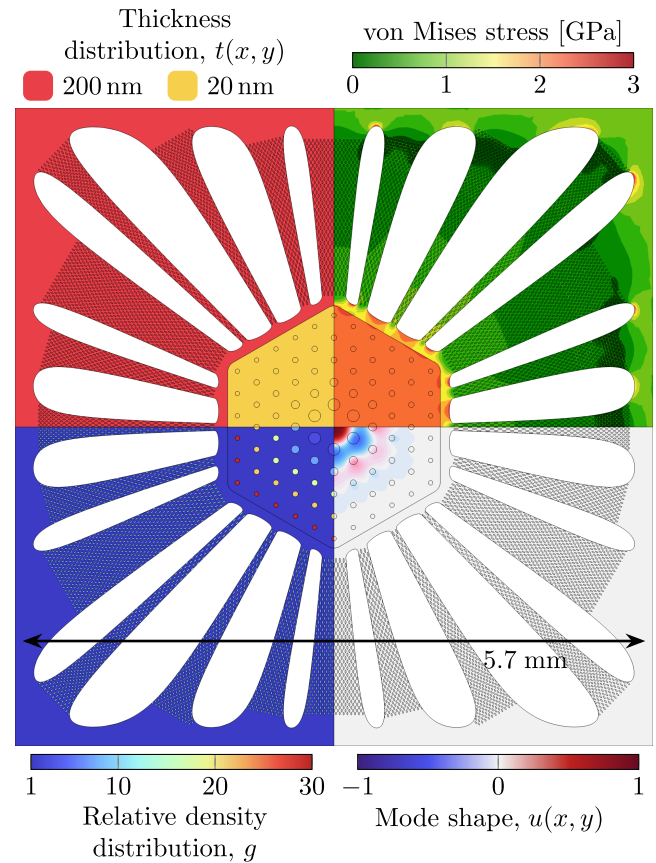


FIG. 4. 2D strain engineering. Schematic representation of a stoichiometric silicon nitride membrane optimized with strain engineering. The central membrane, suspended via thicker tethers, experiences enhanced, uniform tensile stress. To mitigate undesired dissipative vibrations, the tethers are patterned using a stress-modulated density phononic crystal design. This configuration anticipates a quality factor of 3.5×10^9 at 2 MHz room temperature, resulting in a (Qf) product of 7×10^{15} Hz.

nonuniform phononic crystal, which leads to further quality factor improvements while also shrinking the size of the device. An example of this is shown in Fig. 11 in Appendix C. Further improvement is expected by optimizing the density variation using, for example, the mathematical framework of topology optimization.

The deployment of pillars for phononic engineering mirrors previous techniques in photonic crystal engineering, which enabled the creation of high-reflectivity surfaces, as evidenced in trampolines and membranes [9,33]. Our fabrication method is particularly amenable to seamlessly integrating these features into the central defect region. Significantly, computational simulations using the Stanford stratified structure solver [34] reveal that a hexagonal configuration of pillars, characterized by a height of 300 nm, a periodicity of 1500 nm, and a radius of 400 nm, achieves a predicted transmittance near 10^{-9} . The actual transmittance is expected to be orders of magnitude lower due to solver limitations, fabrication-related imperfections,

and the choice of material for the pillars. For instance, nonstoichiometric silicon nitride, including the PECVD variant used in this work, is known for exhibiting absorption. Notably, this design does not compromise the device's intrinsic parameters like effective mass, quality factor, or resonant frequency. Such a configuration offers a promising pathway, enhancing optomechanical coupling and paving the way for novel optomechanical experiments and applications.

In conclusion, we proposed and demonstrated a new method for phononic crystal engineering of micromechanical and nanomechanical membranes that realizes acoustic shielding and soft clamping, and that leaves a lot of flexibility for parameter optimization and strain engineering. The fabricated devices exhibit quality factors as high as 9.1×10^8 at room temperature, and with further optimization of pillar size [see Fig. 2(c)], pattern design [see Fig. 8(b) in Supplemental Material], and strain engineering (see Fig. 4), we anticipate quality factors approaching 1×10^{10} at room temperature. With such quality factors, it is possible to bring the membrane into the quantum ground state at room temperature via feedback cooling (possibly without the use of a cavity) and to eventually prepare nonclassical mechanical states such as squeezed and entangled states with applications in quantum repeaters [35] and sensors. Even more intriguingly, the high quality of our membranes might eventually facilitate the preparation of quantum non-Gaussian mechanical states through the interaction with two-level systems such as defect centers in diamond [36] or superconducting qubits [37], and the realization of quantum transduction to coherently connect two disparate systems with close to unity efficiency [38]. Finally, in the current work, we have focused on the improvement of the quality factor, and the Qf product, which is of high relevance for many of the applications mentioned above. However, in a future work, it would be interesting to optimize the Q/f fraction for applications in atomic force microscopy or optimize the $Q \times m$ product (where m is the effective mass) as required for testing alternative models of quantum mechanics.

II. METHODS

A. Simulations

The simulations of the membranes and nanopillars were performed in COMSOL MULTIPHYSICS. The nanopillars were simulated in full 3D for a single pillar using Floquet periodic boundary conditions. The wave number was defined as $k = 2\pi f \sqrt{g\rho/\sigma}$ (where σ is the tensile stress and f is the frequency) and the damping was extracted in postprocessing by integrating the strains over the entire volume. The loss factor and other material parameters were assumed constant and isotropic. Based on these results, the membranes were modeled in 2D assuming a uniform tensile stress distribution and by adjusting the material

density using $\rho \rightarrow \rho(x, y) = g(x, y)\rho$. The losses in the density-increased domains are scaled based on the chosen pillar periodicity a_{pil} and pillar simulation results. The quality factor $Q = 2\pi W/\Delta W$ is then estimated in post-processing using the kinetic energy,

$$W = 2\pi^2 f^2 t \iint \rho(x, y) u^2(x, y) dx dy, \quad (2)$$

and dissipation via bending,

$$\Delta W = \frac{\pi E t^3}{12(1-\nu^2)} \iint \phi(x, y) \times \left(\frac{\partial^2 u(x, y)}{\partial x^2} + \frac{\partial^2 u(x, y)}{\partial y^2} \right)^2 dx dy, \quad (3)$$

where t , E , and ν are the thickness, Young's modulus, and Poisson's ratio of the resonator material. $u(x, y)$ is the mode shape and $\phi(x, y)$ is the effective loss angle of the membrane, which is affected by the choice of material, its thickness, and the presence of pillars.

B. Fabrication

Three different process flows have been developed to fabricate the density phononic membranes. The simplest and most used process flow is presented here, while more in-depth details of all three different methods can be found in Appendix E. Double-sided polished silicon wafers (of 500 μm thickness) were initially deposited with 20 nm stoichiometric silicon nitride via low-pressure chemical vapor deposition, followed by a layer of about 1000 nm silicon nitride using plasma-enhanced chemical vapor deposition. The pillar pattern was transferred onto a spin-coated layer of photoresist via UV lithography followed by reactive ion etching almost through the PECVD layer. A script was developed to convert any desired nanopillar pattern to a UV-lithography mask file (see Appendix D). Another round of lithography and reactive ion etch was performed on the back side to define the membrane window. Finally, a short etch in buffered hydrofluoric acid followed by an etch in potassium hydroxide ensured the removal of the residual PECVD layer and release of the membrane. The membranes were then cleaned in hydrochloric acid followed by sulfuric acid mixed with ammonium persulfate and later dried in ethanol fumes.

C. Optical characterization

The phononic spectra as well as the Q factors are measured using optical interferometry at 1550 nm. The membrane under study is placed inside a vacuum chamber with pressure $< 10^{-7}$ mbar and excited with a modulated laser beam reflecting off its central part. Once excited, the laser modulation is turned off, and the phase shift of the reflected beam is measured as a function of time with a

phase-locked homodyne detector. The signal is used to record the phononic mode spectrum as well as the amplitude decay of the phase modulation with specific examples shown in Figs. 3(c) and 3(d).

ACKNOWLEDGMENTS

This work has received funding from the Danish National Research Foundation (bigQ DNR142).

APPENDIX A: MASS ENGINEERING OF A MEMBRANE

As discussed in the main text, the dissipation associated with adding mass for enabling phononic crystal engineering can be mitigated by adding the mass in the form of an array of nanopillars. In this appendix, we consider this “dissipation-dilution” effect first for a 1D structure and then for a 2D structure.

The 1D case works well for illustrating the core idea of using mass engineering to define phononic crystals. The speed of propagation in a string is defined by $c = \sqrt{\sigma/\rho}$, where σ and ρ are the string’s tensile stress and material density, respectively. The latter must not be confused with mass in general, since a thicker string will *not* lead to a slower speed of propagation. The material density can be enhanced by adding pillars [Fig. 5(a)] to the string. The pillars add the mass needed but still preserve the low-stress-dominated stiffness since the string can freely bend between the pillars. The effective material ρ_{eff} density is then defined by

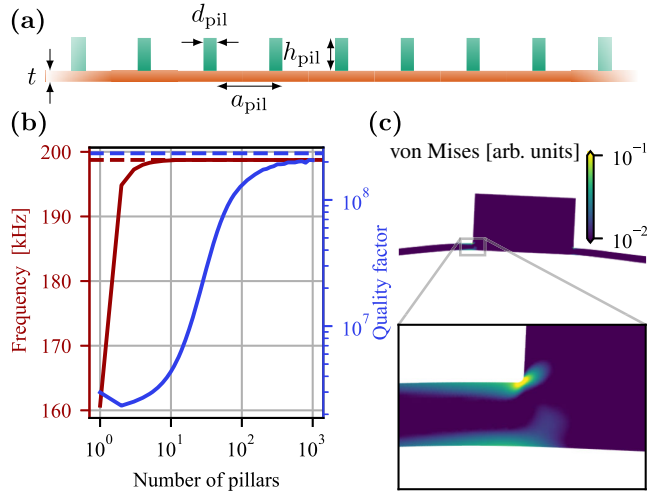


FIG. 5. Illustration of the core design concept for density phononic. (a) A subsection of a string embedded with pillars. (b) Eigenfrequency and quality factor of a simply supported silicon nitride string versus number of pillars uniformly spread along the string. The dashed lines are the solution for a normal string where $\rho \rightarrow \rho_{\text{eff}}$. Plotted for $L = 700 \mu\text{m}$, $t = 50 \text{ nm}$, $\sigma = 1.2 \text{ GPa}$, $d_{\text{pil}} = a_{\text{pil}}/2$ and $\rho_{\text{eff}} = 5\rho$. (c) Highlight of the added bending losses introduced by pillars.

$$\rho_{\text{eff}} = \rho + \rho_{\text{pil}} \frac{h_{\text{pil}} d_{\text{pil}}}{t a_{\text{pil}}}, \quad (\text{A1})$$

where ρ_{pil} is the material density of the pillars themselves and the other parameters are shown in Fig. 5(a).

In Fig. 5(b) we plot the frequency and the quality factor of the string as a function of the number of pillars (for a fixed length of the string). We clearly see that as more pillars are added in an ever finer mesh, the frequency of the density enhanced string quickly approaches the same frequency of a hypothetical string with enhanced material density but without pillars (represented by the dashed line). It is also clear that the introduction of pillars adds additional bending losses at the base [as illustrated in Fig. 5(c)] leading to a lower quality factor of the string. However, fortunately, this loss contribution can be diluted out by defining an even finer mesh of pillars, and thus for a large number of very small pillars the pillar-patterned string will be almost indistinguishable from a hypothetical string without pillars but with enhanced material density.

We now move on to the more interesting case of two-dimensional membranes. For optimal performance of a membrane under high tensile stress using phononic crystals based on mass engineering, the pillars should be patterned as tightly as possible. Naturally, a hexagonal pattern consisting of circular pillars is a good candidate for this, as this allows the pillars to be placed with a high density and the circular shape is among the easiest geometries to fabricate. From Fig. 1(b) the effective material density is then given by

$$\rho_{\text{eff}} = \rho + \rho_{\text{pil}} \frac{\pi\sqrt{3} h_{\text{pil}} d_{\text{pil}}^2}{6 t a_{\text{pil}}^2}, \quad (\text{A2})$$

where t is the thickness of the membrane itself and ρ_{pil} is the material density of the pillars. The above is derived considering the mass contribution from a single pillar and then comparing to the mass contribution from the membrane in a single hexagonal cell. Assuming the same material is used leads to the solution shown in Eq. (1).

As a next step we will consider the distribution of the material density, that is, the phononic crystal pattern. If one assumes a membrane with no holes or features etched into it, the stress will be completely uniform. Far away from any boundaries the physics will then be completely described by a simple isotropic wave equation of the form [39]

$$T' \nabla^2 u(x, y) + m''(x, y) \frac{\partial^2 u(x, y)}{\partial t^2} = p_e(x, y), \quad (\text{A3})$$

where $u(x, y)$ is the out-of-plane displacement of the membrane at point (x, y) , $T' = t\sigma$ is the tensile force per unit length with σ being the tensile stress of the membrane, $m''(x, y) = t\rho_{\text{eff}}(x, y)$ is the mass per unit area of the membrane, and $p_e(x, y)$ is some external pressure distribution. From a mathematical point of view it is very similar to

optical waves, and thus our system's design is a mechanical analog to the common photonic crystal designs. A commonly seen pattern design with good band gap properties is a binary distribution of circular shaped air domains placed on a hexagonal pattern in a dielectric material [40]. The circles represent high phase-velocity domains whereas the surrounding domains are slow phase-velocity. To limit the amount of mass getting added to the membrane, an inverted adaptation of this distribution was studied as well as a softer sinelike distribution to demonstrate the flexibility of this scheme and compare the effects. Both of these are shown in Fig. 6. The binary distribution is defined as

$$\begin{aligned}
 g_{\text{bin},0}(x, y) &= \begin{cases} g_{\text{max}} - 1 & \sqrt{x^2 + y^2} \leq \frac{\alpha_w}{2} a_{\text{ph}} \\ 0 & \text{otherwise,} \end{cases} \\
 g_{\text{bin}}(x, y) &= 1 + g_{\text{bin},0}(x, y) + g_{\text{bin},0}\left(x - \frac{a_{\text{ph}}}{2}, y - \frac{\sqrt{3}a_{\text{ph}}}{2}\right) + g_{\text{bin},0}\left(x + \frac{a_{\text{ph}}}{2}, y - \frac{\sqrt{3}a_{\text{ph}}}{2}\right) \\
 &\quad + g_{\text{bin},0}\left(x - \frac{a_{\text{ph}}}{2}, y + \frac{\sqrt{3}a_{\text{ph}}}{2}\right) + g_{\text{bin},0}\left(x + \frac{a_{\text{ph}}}{2}, y + \frac{\sqrt{3}a_{\text{ph}}}{2}\right), \\
 &\quad \text{for } -\frac{a_{\text{ph}}}{2} \leq x \leq \frac{a_{\text{ph}}}{2} \\
 &\quad \text{and } -\frac{\sqrt{3}a_{\text{ph}}}{2} \leq y \leq \frac{\sqrt{3}a_{\text{ph}}}{2} \\
 g_{\text{bin}}(x, y) &= g_{\text{bin}}(x - na_{\text{ph}}, y - m\sqrt{3}a_{\text{ph}}), \\
 \{n, m\} &= 0, \pm 1, \pm 2, \dots,
 \end{aligned} \tag{A4}$$

and similarly for the sinelike distribution,

$$\begin{aligned}
 g_{\text{sin},0}(x, y) &= \frac{g_{\text{max}} - 1}{2} \left[1 + \cos\left(2\pi \frac{\sqrt{x^2 + y^2}}{\alpha_w a_{\text{ph}}}\right) \right] \\
 &\quad \text{for } \sqrt{x^2 + y^2} \leq \frac{\alpha_w}{2} a_{\text{ph}},
 \end{aligned} \tag{A5}$$

with $g_{\text{sin}}(x, y)$ defined in the same manner as $g_{\text{bin}}(x, y)$. The effective density is then given by $\rho_{\text{eff}}(x, y) = \rho \times g_i(x, y)$, where $i = \{\text{bin}, \text{sin}\}$.

Both of these distributions have a few degrees of freedom. When ignoring the pillars these are the maximum relative effective density g_{max} , the relative distribution width α_w , and the phononic crystal periodicity a_{ph} . These will be explored in Appendix B.

APPENDIX B: OPTIMIZING THE MASS ENGINEERED PHONONIC CRYSTAL

How one eventually chooses to design the mass engineered phononic crystal has a huge effect on how well any modes confined to a defect will end up performing. A wide band gap ensures an efficient isolation of the mode.

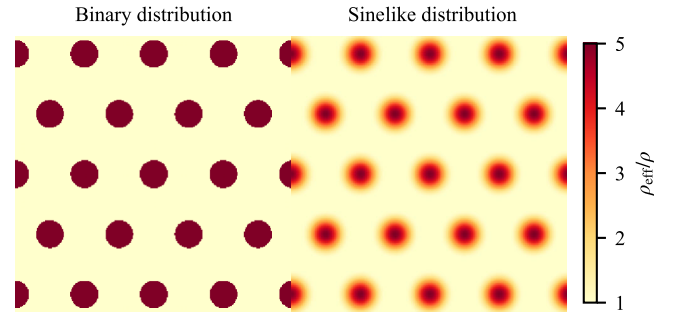


FIG. 6. Examined effective density distributions for two uniform phononic crystals investigated in this study.

However, the distribution must also be designed to minimize additional design-induced losses. Finally, while a large effective density contrast will generate a correspondingly wide band gap, it is also increasingly difficult to fabricate; thus the lowest possible contrast should be used. All these factors were studied for the two proposed distributions presented in Appendix A.

In Fig. 7, a range of parametric sweeps were conducted for the binary effective density distribution. The phononic periodicity a_{ph} was kept constant, as this simply scales the band gap frequency. The remaining parameters are the relative distribution width α_w and the relative effective density maximum g_{max} , which were swept across a meaningful range. For the band gap width it is clear that as the density contrast is increased, the band gap becomes wider as one would expect. There is also clearly an optimum distribution width defined at $\alpha_w \approx 0.4$. However, at the same time the quality factor of a mode passing through a region of increasingly higher densities is reduced. This is a direct consequence of the phase-velocity definition. Higher densities lead to slower velocities and therefore shorter wavelength. This in turn leads to sharper bending of the mode shape and therefore higher losses. This compromise

between band gap and losses is also seen for stress-based phononic devices [41]. Moreover, the center frequency of the band gap is redshifted as the mass of the phononic cell increases, which is to be expected.

How does one then pick the optimal set of parameters for a given density phononic distribution? For ultracoherent resonators, the important figure of merit is the $Q \times f_c$ product, where f_c is the center frequency. Since a wide bandwidth is desirable, a proposed figure of merit for choosing the optimum band gap design is $Q \times f_c \times (\Delta f / f_c) = Q \times \Delta f$. This is also shown in Fig. 7, where a line of optimum solutions can be seen. In fact, based on this definition no improvement of the device can be seen for $g_{\max} \geq 5$. Above this range, the added mass will reduce the quality factor and frequency at the same rate as the band gap is enhanced. Going above $g_{\max} = 5$ then introduces a compromise between strong mode isolation versus high quality factor.

The same study was performed for the sinelike distribution and presented in Fig. 8. Overall, the same conclusions can be drawn. The only significant difference can be seen when comparing the $Q \times \Delta f$ products of the two distributions. They converge to about the same maximum value, but the sinelike distribution reaches this plateau for a broader range of parameters, and it is obtained for a slightly higher g_{\max} just below 6. In general, the sinelike distribution obtains slightly lower losses at the cost of slightly worse band gap widths. The higher g requirement also makes it slightly more difficult to fabricate.

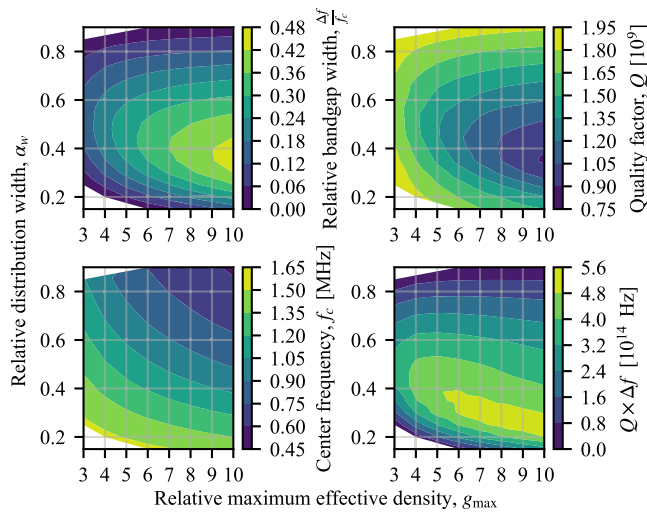


FIG. 7. Study of the binary effective density distribution based phononic crystal. White areas have no band gap defined. Quality factor estimated by taking the mean of the estimated quality factors of the mode just above and just below the band gap. Simulated for $h = 20$ nm, $\sigma = 1.1$ GPa, an intrinsic quality factor of 5860, and $a_{\text{ph}} = 253$ μm .

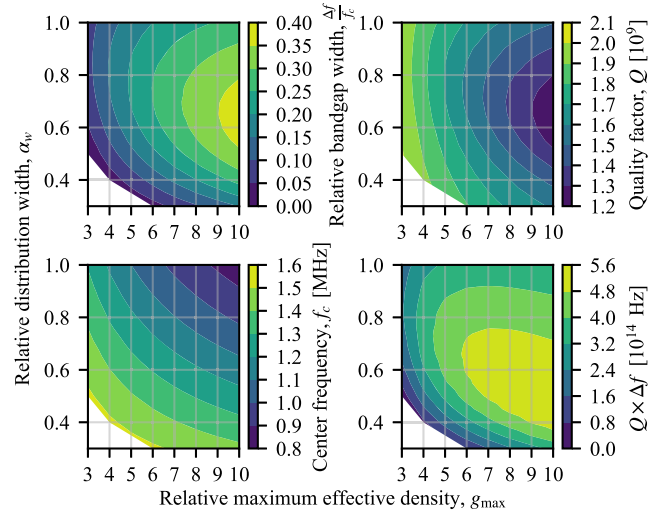


FIG. 8. Study of the sinelike effective density distribution based phononic crystal. White areas have no band gap defined. Quality factor estimated by taking the mean of the estimated quality factors of the mode just above and just below the band gap. Simulated for $h = 20$ nm, $\sigma = 1.1$ GPa, an intrinsic quality factor of 5860, and $a_{\text{ph}} = 260$ μm .

APPENDIX C: MEMBRANE DESIGNS AND ANALYSIS

The subsequent phase of the design process involves leveraging insights from the phononic crystal analysis to formulate full-scale membrane designs. This appendix introduces the developed membrane designs and delves into the engineering of defects to properly confine a mode of interest. A summary of the design types is provided in Table I. The primary designs are the binary and sinusoidal configurations, as elaborated in the main text. Yet, to underscore the versatility of membrane design, we also examine a nonuniform binary distribution.

All of the designs were engineered to have a defect-confined mode at exactly 1.4 MHz at the center of the band gap. The designs and characteristics are shown in Figs. 9 and 10 for the binary and sinelike design, respectively.

The density distribution for the binary design in Fig. 9(a) illustrates how the defect can be implemented. The enhanced density is removed at one of the cells. This disturbance in the lattice is sufficient to confine an eigenmode to the defect. However, the resonance frequency of such a mode is not well centered within the band gap, but instead it is near the lower end of the gap. In order to guarantee maximum mode confinement, the resonance frequency must be shifted to the center of the band gap. This is easily achieved by manipulating the phononic cells right next to the defect. By lowering their effective density slightly, the effective mass of the defect-confined mode is reduced, which results in a higher resonance frequency. Alternatively, one can reduce the size of the high density region of these cells.

TABLE I. Summary of the phononic crystal designs explored in this study. For multiple listed values as v_1, \dots, v_n^T , each value corresponds to a hexagonal ring of cells radiating outward from the central defect: v_1 corresponds to the first ring, v_2 to the second, and so on, with v_n denoting the remaining cells on the membrane.

Design type	α_w	a_{ph}	g
Binary	0.4	198.8 μm	$\{3.9\}$ $\{5.0\}$
Sinelike	0.7	204.3 μm	$\{3.6\}$ $\{5.0\}$
Nonuniform, $N_{ph} = 2$	$\{0.23\}$ $\{0.33\}$	178.5 μm	$\{34.9\}$ $\{58.5\}$
Nonuniform, $N_{ph} = 3$	$\left\{ \begin{array}{l} 0.46 \\ 0.23 \\ 0.44 \end{array} \right\}$	178.5 μm	$\left\{ \begin{array}{l} 2.9 \\ 25.5 \\ 24.0 \end{array} \right\}$
Nonuniform, $N_{ph} = 4$	$\left\{ \begin{array}{l} 0.62 \\ 0.28 \\ 0.46 \\ 0.47 \end{array} \right\}$	178.5 μm	$\left\{ \begin{array}{l} 2.6 \\ 16.5 \\ 22.2 \end{array} \right\}$
Nonuniform, $N_{ph} = 5$	$\left\{ \begin{array}{l} 0.57 \\ 0.36 \\ 0.53 \\ 0.55 \end{array} \right\}$	178.5 μm	$\left\{ \begin{array}{l} 2.6 \\ 8.6 \\ 15.9 \end{array} \right\}$
Nonuniform, $N_{ph} = 6$	$\left\{ \begin{array}{l} 0.57 \\ 0.36 \\ 0.37 \\ 0.38 \end{array} \right\}$	178.5 μm	$\left\{ \begin{array}{l} 2.9 \\ 10.6 \\ 18.1 \end{array} \right\}$
Nonuniform, $N_{ph} = 7$	$\left\{ \begin{array}{l} 0.59 \\ 0.53 \\ 0.39 \\ 0.39 \end{array} \right\}$	178.5 μm	$\left\{ \begin{array}{l} 2.8 \\ 3.9 \\ 7.7 \end{array} \right\}$

Simulations of the defect-confined mode are shown Fig. 9(b) confirming the mode-confining behavior. The band gap for this specific configuration was estimated and shown in Fig. 9(c). An interesting difference between this and what is typically seen for stress phononic band gaps is

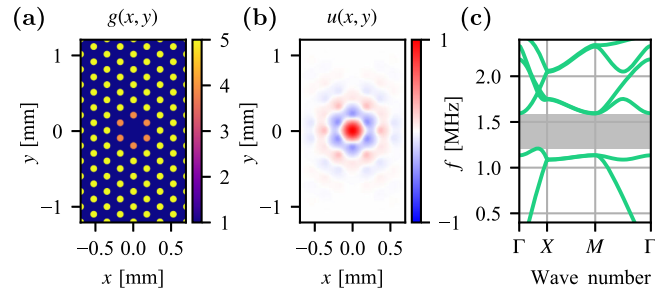


FIG. 9. A study of density phononic membrane using the binary design. (a) Relative effective density distribution near the defect of an infinite membrane. (b) Mode shape of the defect-confined mode at 1.4 MHz. (c) Dispersion relation of the chosen phononic crystal design. The band gap is marked by a shaded region and has a width of $\Delta f = 383$ kHz.

the absence of fast-traveling in-plane modes within the band gap. Stress-based phononic crystals only exhibit pseudo-band gaps [18], whereas the mass engineered phononic crystals exhibit a full band gap. It is known that in-plane modes are unaffected by tensile stress, and therefore stress modulating a membrane or string cannot ever create a band gap for all types of vibrations simultaneously [32]. Conversely, a mass contrast works equally well on all types of vibrations and is likely the reason for the full band gap.

The density distribution for the sinelike design in Fig. 10(a) was designed and manipulated in the exact same manner as for the binary design. The dispersion diagram in Fig. 10(c) shows a somewhat narrower width of the band gap. By comparing the defect-confined mode shape in Fig. 10(b) with the binary design one can (with a sharp eye) see the mode is slightly less confined for the sinelike design.

In contrast to traditional designs, the nonuniform crystal lacks a distinct dispersion relation, given its nonstandard crystal configuration. The guiding principles behind this design are to maximize mode confinement while keeping the bending loss at a minimum. Since most of the mechanical energy is confined around the central defect, it is imperative to minimize damping in this vicinity. Hence the first 1–2 cells should have cells containing only a minimum amount of added mass, as shown in Table I. As we move outward, where bending energy has substantially diminished, there is leeway to amplify the relative density, bolstering mode confinement without accruing significant additional damping. This design paradigm enables the creation of resonators with enhanced quality factors, yet retaining a compact form. To achieve these parameters, the relative density (g) and distribution (α_w) are optimized separately for each hexagonal ring, targeting an optimal (Qf) product. The boundary bending losses are multiplied by 10 to promote mode-shape confinement far away from the outer boundary. An example of one of the generated designs is shown in Fig. 11(a).

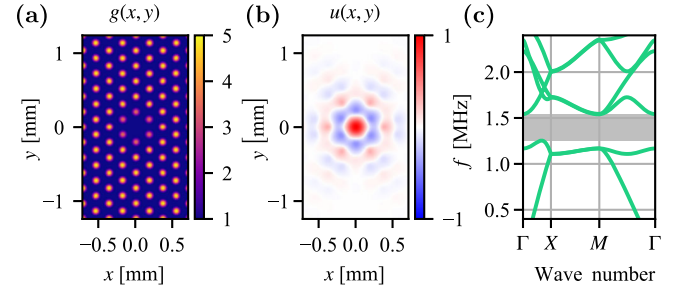


FIG. 10. A study of density phononic membrane using the sinelike design. (a) Relative effective density distribution near the defect of an infinite membrane. (b) Mode shape of the defect-confined mode at 1.4 MHz. (c) Dispersion relation of the chosen phononic crystal design. The band gap is marked by a shaded region and has a width of $\Delta f = 286$ kHz.

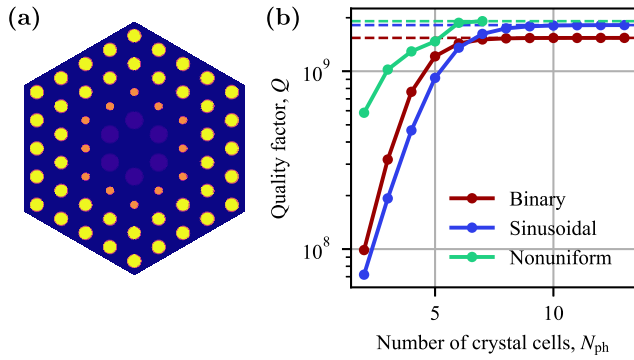


FIG. 11. Evaluating the influence of the number of phononic crystal cells N_{ph} on the intrinsic quality factor. (a) Representative model of a nonuniform crystal design with $N_{\text{ph}} = 4$. (b) Projected quality factors, based on parameters $h = 20$ nm, $\sigma = 1.1$ GPa, and an intrinsic quality factor of 5860. All designs function around 1.4 MHz. Pillar-induced losses are not considered in this assessment.

A critical parameter yet to be addressed is the number of phononic crystal cells required for effective mode confinement, denoted as N_{ph} . This count largely depends on the damping mechanism. For intrinsic losses, adding more crystal cells is essential until bending losses at the clamping points are negligible. Losses due to coupling with the surrounding substrate were not considered. A numerical investigation was conducted to estimate the optimal cell count. The study assumed a hexagonal window, aligning naturally with the lattice, as depicted in Fig. 11(a). The outcomes for both resonator types are presented in Fig. 11(b).

Simulations reveal that the subtle band gap width variation between the binary and sinelike designs influences the requisite number of phononic crystal cells. The binary design necessitates a minimum of $N_{\text{ph}} = 7$ cells, while the sinelike design requires approximately $N_{\text{ph}} = 9$. This seemingly minor disparity can significantly impact fabrication yield, as larger membranes correlate with increased fabrication challenges. Nonetheless, beyond these cell counts, the sinelike design is projected to exhibit a marginally superior quality factor, a conclusion consistent with earlier phononic crystal analyses. The showcased results epitomize the upper predicted threshold achievable with pillars crafted at a finely detailed mesh resolution. Observing the nonuniform crystal designs underscores the feasibility of crafting more compact structures with enhanced quality factors. Exploring other noncrystal designs, potentially employing topology optimization, offers a promising prospect for further advancements in performance or size reduction.

APPENDIX D: DENSITY DISTRIBUTION TO PILLAR LAYOUT CONVERSIONS

A convenient feature of using pillars to alter the effective density of the material is that *any* density distribution can be used and approximated by a sufficiently fine mesh of pillars. A script was written in MATLAB and used on the layout editor CleWin to convert any effective density distribution. The approximated converted layouts for both designs will be presented and discussed.

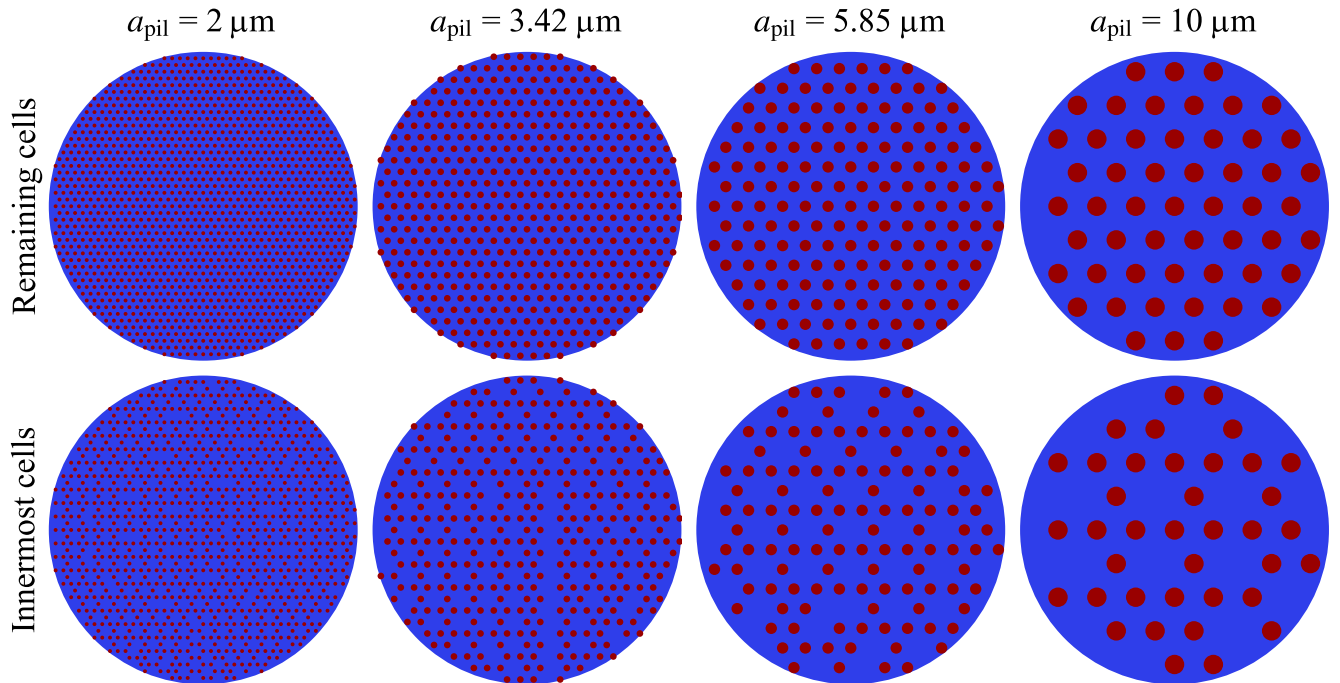


FIG. 12. Effective density distribution (blue background) to pillar layout (red circles) conversions for the binary design for different pillar periodicities a_{pil} . The bottom row are phononic cell layouts with reduced effective density which are placed next to the defect.

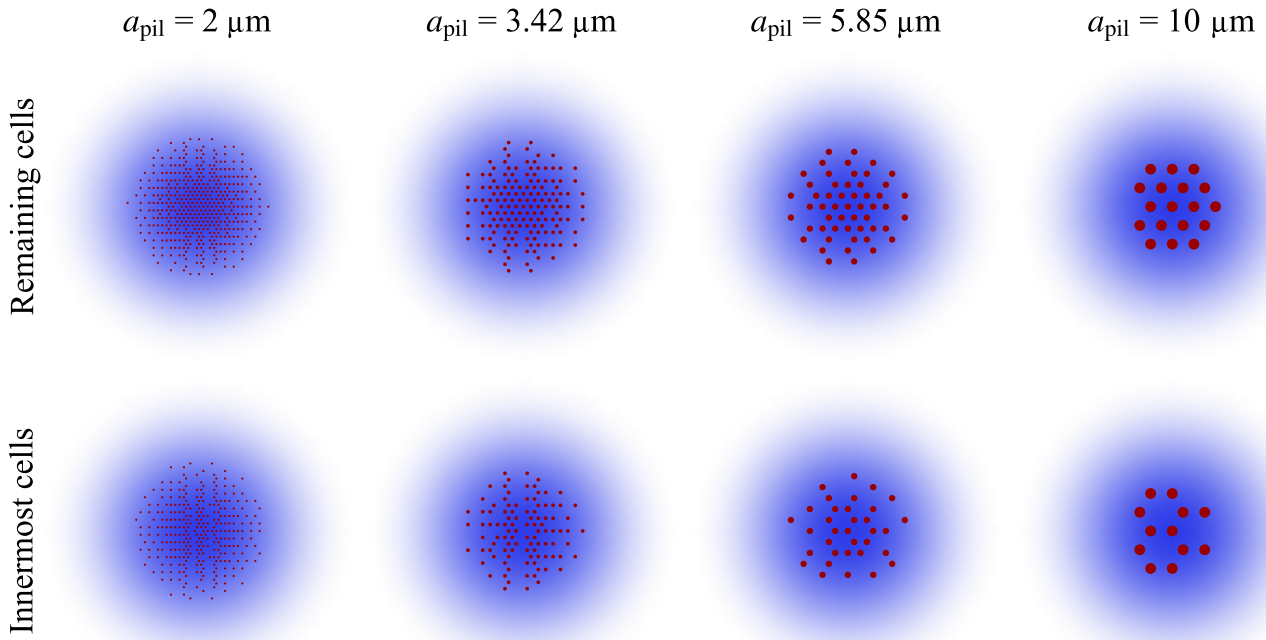


FIG. 13. Effective density distribution (blue background) to pillar layout (red circles) conversions for the sinelike design for different pillar periodicities a_{pil} . The bottom row are phononic cell layouts with reduced effective density which are placed next to the defect.

To simplify fabrication and the mask layout, all pillars were fabricated with the same diameter, height, and resolution on a hexagonal grid. The pillar diameter is set to half the periodicity, $d_{\text{pil}}/2a_{\text{pil}}$. With these parameters fixed the only way to modulate the effective density is by omitting pillars at certain hexagonal coordinates depending on the density defined. This discretization method is naturally an approximation that depends on the resolution of pillars: A finer pillar mesh resolutions will result in a better approximation of the effective density distribution being converted. In all cases, the total added mass matches the original distribution $g(x, y)$ as closely as possible.

The simplest distribution to convert is the binary distribution shown in Fig. 12 for pillar periodicities used in fabrication. Finer resolutions are of course possible, but for normal UV lithography 1 μm features are about the smallest structures which can be fabricated reliably. The top row represents the regular pillar distributions of the cells for different pillars size, while the bottom row illustrates the results of the cells with reduced effective density, by means of missing pillars. The corresponding layout for the more complicated sinelike distribution is shown in Fig. 13. The continuous density distribution is approximated by a high density of pillars in the center which gradually become less dense away from the center. Here it is clear that a finer mesh resolution does a significantly better job at replicating the sinelike distribution.

In the current work, we have fabricated and experimentally characterized the binary distribution design. The fabrication procedure is discussed in Appendix E, and

the experimental characterization procedure and results are presented in the main text.

APPENDIX E: FABRICATION

Three distinctive fabrication processes for these devices have evolved over time, all employing 500 μm double-sided polished Si wafers. These processes are comprehensively detailed below and visualized in Fig. 14.

1. Process flow 1: Initial successful approach

This method marked our first successful batches, and the majority of subsequent results draw from this foundational work. The fabrication begins with the coating of wafers with a 20 nm layer of stoichiometric silicon nitride using low-pressure chemical vapor deposition (LPCVD). Following this, an additional 1000 nm layer of silicon nitride is applied using plasma-enhanced chemical vapor deposition. To form the pillar pattern, a spin-coated photoresist layer undergoes UV lithography and is then almost completely etched through the PECVD layer with reactive ion etching (RIE). The back side of the wafer is then detailed with another round of lithography and RIE to define the membrane window. A brief exposure to buffered hydrofluoric acid (BHF) is applied next. The process concludes with a potassium hydroxide (KOH) treatment, effectively removing any lingering PECVD layer and releasing the membrane. Following this, the membranes are cleaned using hydrochloric acid, treated with a

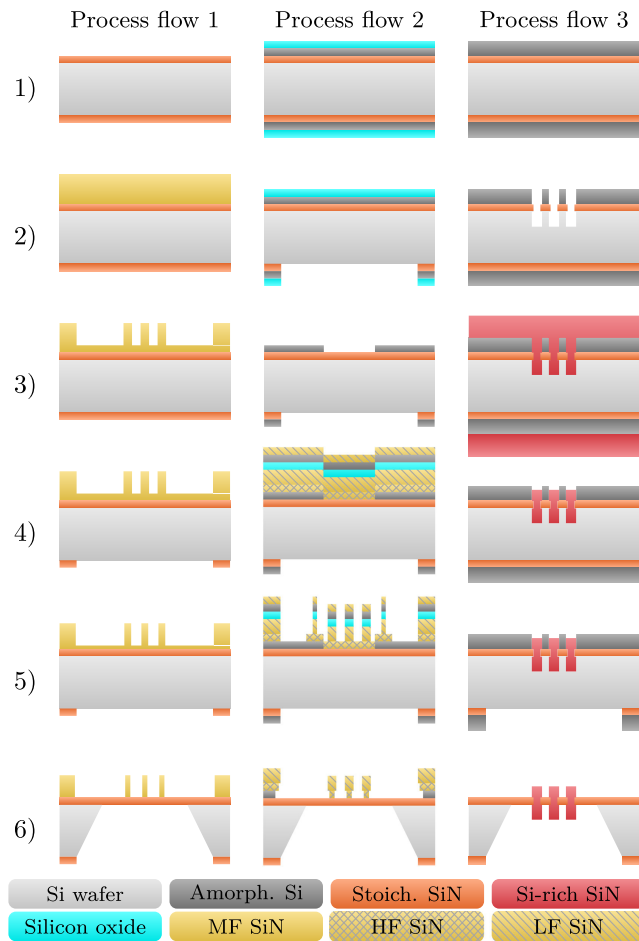


FIG. 14. Illustrations of the three different process flows developed over time for fabricating the devices. The MF SiN, HF SiN, and LF SiN refer to PECVD processes of silicon nitride using mixed-frequency, high-frequency, and low-frequency deposition plasma, respectively. See main text for more details on each step. Note that none of the illustrations reflect real dimensions or patterns.

combination of sulfuric acid and ammonium persulfate, and finally dried in ethanol fumes.

2. Process flow 2: Refined approach

To enhance the etching precision of the pillars, we revised the previous method and implemented it in subsequent samples. The initial phase involves depositing a 20 nm layer of stoichiometric silicon nitride, amorphous silicon, and tetraethoxysilane-based silicon oxide onto the wafers using the LPCVD technique. Here, the amorphous silicon layer serves a dual purpose: acting as a lift-off mask to eliminate unwanted pillars, and the oxide layer is specially designed as a KOH-resistant mask for this amorphous silicon layer.

In the subsequent stage, the design for the back side membrane window's KOH etch mask is mapped onto a spin-coated photoresist layer. This is achieved through UV lithography, followed by an RIE that penetrates the silicon

nitride layer. Afterward, the resist is dissolved using an oxygen plasma. To further refine the design, another round of lithography is executed on the wafer's top side to establish the lift-off pattern. This is succeeded by RIE targeting the oxide layer. Once this is done, the resist is removed with oxygen plasma, and a brief KOH etching is employed to clear away any exposed segments of the amorphous silicon layer. A rapid BHF etch subsequently ensures the removal of the oxide layer.

Next is a series of PECVD steps. A thin base layer of high-frequency deposited silicon nitride followed by low-frequency deposited silicon nitride. The high-frequency layer etches much faster than the low-frequency layer in BHF and KOH. This contrast makes it possible to easily remove the residual layer on the membrane while still preserving most of the mass of the pillars. The depositions continue with silicon oxide, amorphous silicon, and silicon nitride. The silicon layer here acts as a hard mask in the following RIE step. The silicon oxide layer should not be needed, but it seems to improve the amorphous Si deposition result. The silicon nitride layer thickness is engineered to minimize UV reflection in the following lithography step.

A final round of top side lithography for the pillar pattern is performed. When transferring the pillar pattern to the photoresist layer, each phononic cell is defined larger than desired, so the pillar mesh pattern extends into the amorphous silicon layer. Since the exposure dose (and therefore pillar diameter) is lower for the outermost pillars, these bad pillars can easily be removed during the back side KOH etch step later in a lift-off fashion.

To wrap up the process, the pillar design is replicated onto the silicon nitride layers via RIE, after which the photoresist is eradicated using oxygen plasma. In the final phase, the wafers are treated with KOH, thoroughly cleaned, and then dried, mirroring the procedures of our initial method.

3. Process flow 3: Pillars as nails

The inherent limitation of the earlier two methodologies arises from the pitch of the pillar mesh. This pitch is restricted due to the isotropic KOH etching of the pillars during the final stages. Achieving offsets for submicron diameters becomes increasingly challenging. A novel method to address this is by etching holes through the membrane layer, subsequently filling them with Si-rich silicon nitride using an LPCVD technique. Owing to its almost infinite selectivity to KOH and the standard RIE processes' capability to etch minuscule holes, this technique offers superior control over the pillars' dimensions. This means fabricating a more refined mesh of pillars well within the submicron range becomes feasible.

Initially, wafers are treated with a 20 nm layer of stoichiometric silicon nitride, succeeded by 250 nm amorphous silicon through LPCVD processes. Following this,

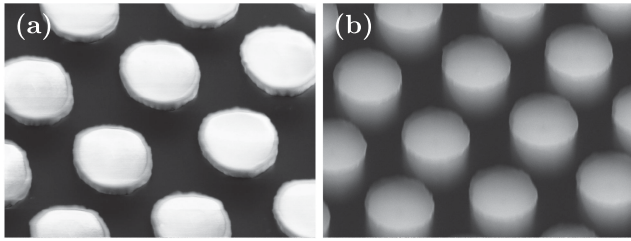


FIG. 15. SEM imaging of pillars using process flow 3. Panel (a) is a low eV image to visualize the top part of the pillars above the membranes and (b) is a high eV image to make the membrane transparent enabling imaging of whole pillars. Taken at a 45° angle. Pattern periodicity is $a_{\text{pil}} = 2 \mu\text{m}$.

the pillar design is projected onto a spin-coated photoresist layer using UV lithography, which is then developed and subjected to RIE. It is crucial that the etching permeates at least the silicon nitride layer since the depth directly affects each pillar's added mass. Once the resist is removed with oxygen plasma, the wafers undergo a brief BHF etch, and subsequently, a short KOH etch at ambient temperature. This results in a slight expansion of the holes' diameter both beneath and above the silicon nitride layer, a factor that becomes evident later on. The wafers are then cleaned with an RCA clean procedure and treated with a substantial 700 nm layer of Si-rich silicon nitride via LPCVD. Subsequently, any superfluous Si-rich silicon nitride is eliminated from both wafer sides through an unmasked RIE procedure, utilizing the amorphous silicon layer as an etch stop. A subsequent round of lithography and reactive ion etching is conducted on the back side to delineate the membrane window. To conclude, the wafers are treated with KOH, purified, and dried in a manner akin to the original process flow.

The culmination of these processes is membranes adorned with nail-like pillars piercing through them. The unique feature of these “nails” is their secure placement owing to the slightly wider diameters above and below the membrane, in contrast to the hole diameter defined by the preliminary RIE step. This methodology boasts a yield of approximately 37% (181 out of 488) for membranes with a side length of 4 mm and $N_{\text{ph}} = 8$ cells insulating the central defect. The pillars produced are consistently well defined, as illustrated in Fig. 15. Furthermore, integrating this approach with the nonuniform crystal design is straightforward. By selectively exposing and etching the holes of specific phononic crystal cells sequentially, regions with varied relative densities g can be crafted.

- [1] S. Barzanjeh, A. Xuereb, S. Gröblacher, M. Paternostro, C. A. Regal, and E. M. Weig, *Optomechanics for quantum technologies*, *Nat. Phys.* **18**, 15 (2022).
 [2] J. Manley, M. D. Chowdhury, D. Grin, S. Singh, and D. J. Wilson, *Searching for vector dark matter with an*

- optomechanical accelerometer*, *Phys. Rev. Lett.* **126**, 061301 (2021).
 [3] S. Nimmrichter, K. Hornberger, and K. Hammerer, *Optomechanical sensing of spontaneous wave-function collapse*, *Phys. Rev. Lett.* **113**, 020405 (2014).
 [4] T. Westphal, H. Hepach, J. Pfaff, and M. Aspelmeyer, *Measurement of gravitational coupling between millimeter-sized masses*, *Nature (London)* **591**, 225 (2021).
 [5] R. Delaney, M. D. Urney, S. Mittal, B. M. Brubaker, J. M. Kindem, P. S. Burns, C. A. Regal, and K. W. Lehnert, *Superconducting-qubit readout via low-backaction electro-optic transduction*, *Nature (London)* **606**, 489 (2022).
 [6] S. S. Verbridge, J. M. Parpia, R. B. Reichenbach, L. M. Bellan, and H. G. Craighead, *High quality factor resonance at room temperature with nanostrings under high tensile stress*, *J. Appl. Phys.* **99**, 124304 (2006).
 [7] S. Schmid, K. D. Jensen, K. H. Nielsen, and A. Boisen, *Damping mechanisms in high-Q micro and nanomechanical string resonators*, *Phys. Rev. B* **84**, 165307 (2011).
 [8] C. Reinhardt, T. Müller, A. Bourassa, and J. C. Sankey, *Ultralow-noise SiN trampoline resonators for sensing and optomechanics*, *Phys. Rev. X* **6**, 021001 (2016).
 [9] R. A. Norte, J. P. Moura, and S. Gröblacher, *Mechanical resonators for quantum optomechanics experiments at room temperature*, *Phys. Rev. Lett.* **116**, 147202 (2016).
 [10] L. G. Villanueva and S. Schmid, *Evidence of surface loss as ubiquitous limiting damping mechanism in SiN micro- and nanomechanical resonators*, *Phys. Rev. Lett.* **113**, 227201 (2014).
 [11] E. Romero, V. M. Valenzuela, A. R. Kermany, L. Sementilli, F. Iacopi, and W. P. Bowen, *Engineering the dissipation of crystalline micromechanical resonators*, *Phys. Rev. Appl.* **13**, 044007 (2020).
 [12] D. Høj, F. Wang, W. Gao, U. B. Hoff, O. Sigmund, and U. L. Andersen, *Ultra-coherent nanomechanical resonators based on inverse design*, *Nat. Commun.* **12**, 5766 (2021).
 [13] A. Beccari, D. A. Visani, S. A. Fedorov, M. J. Beryhi, V. Boureau, N. J. Engelsens, and T. J. Kippenberg, *Strained crystalline nanomechanical resonators with ultralow dissipation*, *Nat. Phys.* **18**, 436 (2021).
 [14] J. R. Pratt, A. R. Agrawal, C. A. Condos, C. M. Pluchar, S. Schlamminger, and D. J. Wilson, *Nanoscale torsional dissipation dilution for quantum experiments and precision measurement*, *Phys. Rev. X* **13**, 011018 (2023).
 [15] D. Shin, A. Cupertino, M. H. J. de Jong, P. G. Steeneken, M. A. Bessa, and R. A. Norte, *Spiderweb nanomechanical resonators via Bayesian optimization: Inspired by nature and guided by machine learning*, *Adv. Mater.* **34**, 2106248 (2022).
 [16] M. Beryhi, A. Beccari, R. Groth, S. A. Fedorov, A. Arabmoheghi, T. J. Kippenberg, and N. J. Engelsens, *Hierarchical tensile structures with ultralow mechanical dissipation*, *Nat. Commun.* **13**, 3097 (2022).
 [17] M. J. Beryhi, A. Arabmoheghi, A. Beccari, S. A. Fedorov, G. Huang, T. J. Kippenberg, and N. J. Engelsens, *Perimeter modes of nanomechanical resonators exhibit quality factors exceeding 10^9 at room temperature*, *Phys. Rev. X* **12**, 021036 (2022).

- [18] Y. Tsaturyan, A. Barg, E. S. Polzik, and A. Schliesser, *Ultracoherent nanomechanical resonators via soft clamping and dissipation dilution*, *Nat. Nanotechnol.* **12**, 776 (2017).
- [19] A. H. Ghadimi, D. J. Wilson, and T. J. Kippenberg, *Radiation and internal loss engineering of high-stress silicon nitride nanobeams*, *Nano Lett.* **17**, 3501 (2017).
- [20] P.-L. Yu, K. Cicak, N. S. Kampel, Y. Tsaturyan, T. P. Purdy, R. W. Simmonds, and C. A. Regal, *A phononic bandgap shield for high- Q membrane microresonators*, *Appl. Phys. Lett.* **104**, 023510 (2014).
- [21] Y. Tsaturyan, A. Barg, A. Simonsen, L. G. Villanueva, S. Schmid, A. Schliesser, and E. S. Polzik, *Demonstration of suppressed phonon tunneling losses in phononic bandgap shielded membrane resonators for high- Q optomechanics*, *Opt. Express* **22**, 6810 (2014).
- [22] A. Ghadimi, D. J. Wilson, and T. J. Kippenberg, *Radiation and internal loss engineering of high-stress silicon nitride nanobeams*, *Nano Lett.* **17**, 3501 (2017).
- [23] A. H. Ghadimi, S. A. Fedorov, N. J. Engelsen, M. J. Breyhi, R. D. Schilling, D. J. Wilson, and T. J. Kippenberg, *Elastic strain engineering for ultralow mechanical dissipation*, *Science* **360**, 764 (2018).
- [24] M. Maldovan, *Sound and heat revolutions in phononics*, *Nature (London)* **503**, 209 (2013).
- [25] T. Vasileiadis, J. Varghese, V. Babacic, J. Gomis-Bresco, D. N. Urrios, and B. Graczykowski, *Progress and perspectives on phononic crystals*, *J. Appl. Phys.* **129**, 160901 (2021).
- [26] A. Song, J. Li, C. Shen, T. Chen, and S. A. Cummer, *Switchable directional sound emission with improved field confinement based on topological insulators*, *Appl. Phys. Lett.* **117**, 043503 (2020).
- [27] M. H. J. de Jong, M. A. ten Wolde, A. Cupertino, P. G. Steeneken, and R. A. Norte, *Mechanical dissipation by substrate-mode coupling in SiN resonators*, *Appl. Phys. Lett.* **121**, 032201 (2022).
- [28] M. Rossi *et al.*, *Measurement-based quantum control of mechanical motion*, *Nature (London)* **563**, 53 (2018).
- [29] D. Mason, J. Chen, M. Rossi, Y. Tsaturyan, and A. Schliesser, *Continuous force and displacement measurement below the standard quantum limit*, *Nat. Phys.* **15**, 745 (2019).
- [30] J. Chen, M. Rossi, D. Mason, and A. Schliesser, *Entanglement of propagating optical modes via a mechanical interface*, *Nat. Commun.* **11**, 943 (2020).
- [31] G. I. Gonzalez and P. R. Saulson, *Brownian motion of a mass suspended by an anelastic wire*, *J. Acoust. Soc. Am.* **96**, 207 (1994).
- [32] S. A. Federov, N. J. Engelsen, A. H. Ghadimi, M. J. Breyhi, R. Schilling, D. J. Wilson, and T. J. Kippenberg, *Generalized dissipation dilution in strained mechanical resonators*, *Phys. Rev. B* **99**, 054107 (2019).
- [33] G. Enzian, Z. Wang, A. Simonsen, J. Mathiassen, T. Vibel, Y. Tsaturyan, A. Tagantsev, A. Schliesser, and E. S. Polzik, *Phononically shielded photonic-crystal mirror membranes for cavity quantum optomechanics*, *Opt. Express* **31**, 13040 (2023).
- [34] V. Liu and S. Fan, *S⁴: A free electromagnetic solver for layered periodic structures*, *Comput. Phys. Commun.* **183**, 2233 (2012).
- [35] N. Fiaschi, B. Hensen, A. Wallucks, R. Benevides, J. Li, T. P. M. Alegre, and S. Gröblacher, *Optomechanical quantum teleportation*, *Nat. Photonics* **15**, 817 (2021).
- [36] D. Lee, K. W. Lee, J. V. Cady, P. Ovarthaiyapong, and A. C. B. Jayich, *Topical review: Spins and mechanics in diamond*, *J. Opt.* **19**, 033001 (2017).
- [37] A. Clerk, K. W. Lehnert, P. Bertet, J. R. Petta, and Y. Nakamura, *Hybrid quantum systems with circuit quantum electrodynamics*, *Nat. Phys.* **16**, 257 (2020).
- [38] N. Lauk, N. Sinclair, S. Barzanjeh, J. P. Covey, M. Saffman, M. Spiropulu, and C. Simon, *Perspectives on quantum transduction*, *Quantum Sci. Technol.* **5**, 020501 (2020).
- [39] S. Schmid, L. G. Villanueva, and M. L. Roukes, *Fundamentals of Nanomechanical Resonators* (Springer, Cham, 2016), pp. 1–175.
- [40] J. D. Joannopoulos, S. G. Steven, J. N. Winn, and R. D. Meade, *Photonic Crystals: Molding the Flow of Light*, 2nd ed. (Princeton University Press, Princeton, 2008), pp. 1–304.
- [41] C. Reetz, R. Fischer, G. G. Assumpção, D. P. McNally, P. S. Burns, J. C. Sankey, and C. A. Regal, *Analysis of membrane phononic crystals with wide band gaps and low-mass defects*, *Phys. Rev. Appl.* **12**, 044027 (2019).